ADVANCED FUNCTIONAL MATERIALS
www.afm-journal.de

Tin-Based 2D/3D Perovskite Vertical Heterojunction for High-Performance Synaptic Phototransistors

*Hok-Leung Loi, Tianyue Wang, Dapeng Liu, Jiupeng Cao, Jing Zhuang, Zeyu Zhao, Yang Xu, Mitch Guijun Li, Liang Li, Tianyou Zhai, and Feng Yan**

There is considerable interest in photodetectors based on nontoxic lead-free perovskites. Tin-based perovskites have been regarded as one type of the most promising candidate materials for these devices due to their relatively low bandgap and high light absorption coefficient. In this work, a stacked 2D/3D heterostructure in perovskite films is achieved through a convenient vacuum drying process, which results in an ultrahigh responsivity of up to 6.8 × 10^5 A W^{-1} and a high detectivity up to 4.0 × 10^{14} Jones at a low gate voltage of −5 V across a broad wavelength region from ultraviolet to near-infrared. Remarkably, the device exhibits synaptic behavior, as demonstrated by its photocurrent response to both photonic and electric stimuli, which closely resembles the memory behavior observed in biological neural networks, promising applications in opto-synaptic devices.

1. Introduction

Photodetectors are essential optoelectronic devices that are used to convert light into electrical signals. Near-infrared (NIR) photodetectors can find widespread use in various industrial and medical applications such as security, environmental monitoring,[1] night vision,[2] tomography,[3] and real-time diagnosis.[4–7] However, the fabrication of conventional NIR photodetectors based on typical inorganic narrow-bandgap materials, including GaAs, PbSe, and InGaAs,[6,8–12] are not very convenient and incompatible with a low-temperature process, which limits their applications in many emerging fields, like flexible/wearable electronics and bioelectronics. Notably, organic-inorganic metal halide perovskites with tunable absorption edges from UV to NIR can be processed using low-cost and all-solution methods at low temperatures. To improve the stability of conventional 3D perovskites, 2D perovskite materials have been introduced in perovskite layers to form 2D/3D mixed perovskites.[13–18] The structural formula for 3D perovskites is ABX_3, while 2D layered Ruddlesden-Popper perovskite materials have a more complex formula of $(A')_2A_{n-1}B_nX_{3n+1}$ (n = 1, 2, 3.....).[19–21] Here, A′ denotes an organic spacer cation, A, B and X represent monovalent cation, divalent metal cation and monovalent halide anion (e.g., $(PEA)_2(FA)_{n-1}Sn_nI_{3n+1}$), respectively. Notably, Ruddlesden-Popper 2D perovskites have large organic cations (e.g., PEA^+) that may act as protective layers to prevent moisture and oxygen from entering the bulk.[13–17] Furthermore, 2D perovskite films consist of n number of $[MX_6]^{4-}$ octahedral layers within each quantum well, offering the potential to adjust their optoelectronic properties.[22–25] Notably, quasi-2D perovskites are generally characterized by the n value larger than 3 (e.g., n = 4, 5, 6...), whereas 2D perovskites are defined by the n ≤ 3 series.[26–28] Although pure 2D Pb-based perovskite photodetectors typically show responsivities below 10 A W^{-1},[29–31] a photodetector with a suitable 2D/3D perovskite vertical heterojunction $(PEA)_2(MA)_{n-1}Pb_nI_{3n+1}$, prepared by hot-casting, has demonstrated a relatively high responsivity of 149 A W^{-1}.[32] However, these lead-based perovskites are toxic and have limitations in their practical applications.[33,34] Hence, we need to develop photodetectors based on lead-free perovskites, such as tin-based perovskites. Among tin-based perovskite materials, $FASnI_3$ has emerged as a promising candidate material for NIR photodetectors due to its relatively low

H.-L. Loi, T. Wang, D. Liu, J. Cao, J. Zhuang, Z. Zhao, F. Yan
Department of Applied Physics
The Research Center for Organic electronics
The Hong Kong Polytechnic University
Hung Hom, Kowloon, Hong Kong 000, P. R. China
E-mail: apafyan@polyu.edu.hk
Y. Xu, M. G. Li
Division of Integrative Systems and Design
Department of Electronic and Computer Engineering
The Hong Kong University of Science and Technology
Clear Water Bay, Kowloon, Hong Kong 000, P. R. China
L. Li
Key Laboratory of Materials Physics
Institute of Solid State Physics
Hefei Institutes of Physical Science
Chinese Academy of Sciences
Hefei 230031, P. R. China
T. Zhai
State Key Laboratory of Materials Processing and Die & Mould Technology
School of Materials Science and Engineering
Huazhong University of Science and Technology
Wuhan 430074, P. R. China
F. Yan
Research Institute of Intelligent Wearable Systems
The Hong Kong Polytechnic University
Hung Hom, Kowloon, Hong Kong 000, P. R. China

The ORCID identification number(s) for the author(s) of this article can be found under https://doi.org/10.1002/adfm.202422267

DOI: 10.1002/adfm.202422267

bandgap (E_g) and high light absorption coefficient.[35] Devices made with $FASnI_3$ have exhibited exceptional optoelectronic properties along with light absorption edges that extend into the NIR region.[36–38] Our group have developed a low-voltage photodetector based on a single layer of p-type 3D Sn-based perovskite film, which exhibits excellent optoelectronic properties and high carrier mobility, leading to a responsivity of 10^5 A W^{-1}.[36] To further improve the performance of perovskite phototransistors, 2D/3D tin-based perovskites can be used as the active layer, which has not been reported until now.

Human intelligence, renowned for its memory and cognition capabilities, functions as an exceptionally efficient information-processing system proficient in complex computational tasks. Thus, brain-inspired computing has emerged as a highly promising paradigm within the realm of artificial intelligence. This approach offers the potential to emulate essential biological functions, including multifunctional sensing and comprehensive signal processing that encompasses transmission, storage, and feedback mechanisms.[39–41] Within this context, the advent of electronic synapses, exemplified by two-terminal memristors and three-terminal transistors, has facilitated the emulation of biological synapses by leveraging their comparable transmission characteristics.[42–45] Furthermore, the nascent field of neuromorphic photonics, which integrates photonics and neuroscience, has provided a compelling avenue for constructing computing systems that amalgamate the efficiency of neural networks with the swiftness of photonics.[46–48] Perovskite synaptic photodetectors have garnered significant attention in recent years for their significant potential in addressing the critical requirement of simultaneous information transmission, a vital aspect underlying memory retention and learning processes within the human brain.[49–51] Notably, lead-free perovskite phototransistors have emerged as promising alternatives for artificial synapses, owing to their notable attributes such as ion migration properties, low toxicity, cost-effective synthesis, and scalability.[40] These devices hold broad application prospects across diverse domains, ranging from wearable artificial intelligence electronic devices to future innovative solutions involving the transplantation of devices into the human body to replace damaged neurons.

In this work, we synthesized a gradient 2D/3D tin-based perovskite vertical heterojunction through an anti-solvent method involving a vacuum treatment of as-deposited perovskite precursor films prior to annealing,[52] which promotes a photogating effect of the perovskite films due to charge separation at the 2D and 3D interfaces in the perovskite channels. Next, a three-step solution-processed passivation process is employed on the film surface to remove some defects in the perovskite channels. The optimized phototransistor exhibits exceptional performance, with a high responsivity of 6.8×10^5 A W^{-1} and gain of 1.1×10^6 in the NIR region. The perovskite device can mimic the neuromorphic learning and remembering behaviors to light stimulation that are characteristic of biological synapses. This work demonstrates the great potential of the 2D/3D Sn-based perovskites in synaptic optoelectronic applications.

2. Results and Discussion

2.1. Film Preparation of 2D/3D Perovskites

To prepare 2D/3D vertical heterojunction perovskite thin films, an anti-solvent method followed by vacuum drying process has been employed, using precursor solutions consisting of PEAI, FAI, and SnI_2 in a mixed DMSO/DMF solvent. As illustrated in **Figure 1a**, 80 µL of perovskite precursor solution with GuaSCN and SnF_2 additives is dripped onto the center of a substrate, followed by a one-step spin-coating process. GuaSCN was used to enhance the crystallinity of the 2D perovskite phase in the 2D/3D heterostructure due to an oriented growth process for the 2D phase resulted from the coordination between SCN^- and Sn^{2+}.[52,53] Moreover, the film quality could be improved as SCN^- ions contribute to the enhancement of grain morphology.[54,55] After ≈30 s, 300 µL of chlorobenzene is quickly deposited onto the coated film to remove redundant DMSO/DMF solvent for better crystallization. The resulting sample is immediately placed in a chamber for 8 min with a pressure of $\approx 10^{-2}$ bar and then annealed at 70 °C for 10 min.

To improve the quality of the perovskite film, a supplemental surface passivation process has been performed in three steps, primarily aimed at eliminating dangling bonds, as shown in Figure 1b. In the first cleaning (C) step, a nonpolar cyclohexane/polar tert-amyl alcohol (CT) solvent is used to remove weakly bonded defective species from the perovskite film.[56] Next, the sample is immersed into the healing (H) solution containing an organic passivating agent (FA^+) in CT solvent to fix any vacancies or organic-halogen defects potentially induced by the previous cleaning approach. Finally, a new cleaning solvent is used to remove residual ionic species from the healing solution and further improve the crystallinity of the perovskite thin film,[57,58] followed by another vacuum drying of 10 min. This surface passivation process, called C—H—C treatment, dramatically improved the quality of perovskites and the performance of perovskite phototransistors consequently, which will be addressed in the later part of the study.

X-ray diffraction (XRD) measurement was conducted to examine the film structure of the perovskite phototransistors. When utilizing a 2D perovskite precursor with a low n value (*e.g.*, n = 1 and 2), there is a thermodynamic preference for the formation of a layered 2D phase rather than the 3D phase.[59–61] This preference is primarily attributed to the insufficient molar ratio of FAI in the $PEA_2FA_{n-1}Sn_nI_{3n-1}$ precursor.[62] Consequently, XRD data of the n = 2 $PEA_2FASn_2I_7$ (2D) perovskite thin film (Figure S1a, Supporting Information) did not display the pronounced 3D component, particularly the (100) and (200) peaks located at 14.0° and 28.2°. Notably, these crystal preferential planes have been distinctly observed in XRD patterns from our $FASnI_3$ (3D) perovskite thin film, as depicted in Figure S1b (Supporting Information), aligning with the characteristics of the reported 3D perovskite structure.[63–66] Notably, in the perovskite film prepared by n = 10 $PEA_2FA_9Sn_{10}I_{31}$ precursor, 3D diffraction patterns were observed along with an additional 2D diffraction peak (n = 2) at ≈3.6°,[67] indicating a 2D/3D perovskite heterojunction (**Figure 2a**).

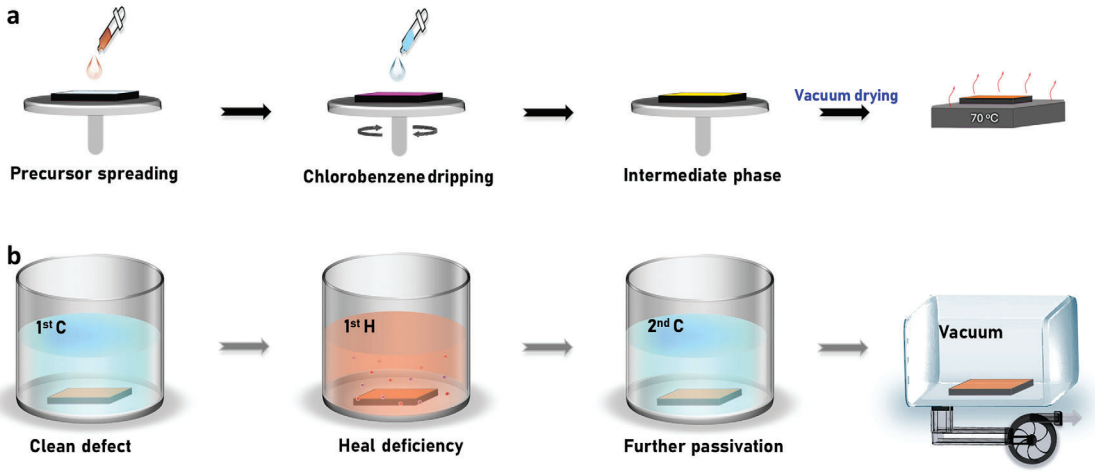

Figure 1. Fabrication process of perovskite films. a) Schematic illustration of perovskite film deposition via an anti-solvent strategy. b) Schematic illustration of surface treatment of a perovskite layer by defect cleaning, healing, and passivation.

Notably, as depicted in Figure S2 (Supporting Information), Sn^{2+} (location at 486.3 and 494.8 eV) appears to dominate the perovskite film surface,[68–70] while Sn^{4+} is notably absent. This observation can be primarily attributed to the excellent anti-oxidation effect of SnF_2 additives at a molar ratio of 10%. Additionally, Sn powder was introduced into the perovskite precursors to facilitate a redox reaction ($Sn^{4+} + Sn \rightarrow 2Sn^{2+}$), which has been filtered before the spin-coating process. To obtain a more precise understanding of the component distribution in the low-dimensional perovskite thin film prepared by the $PEA_2FA_9Sn_{10}I_{31}$ precursor, depth profiling was conducted using Time-of-Flight Secondary Ion Mass Spectrometry (TOF SIMS).

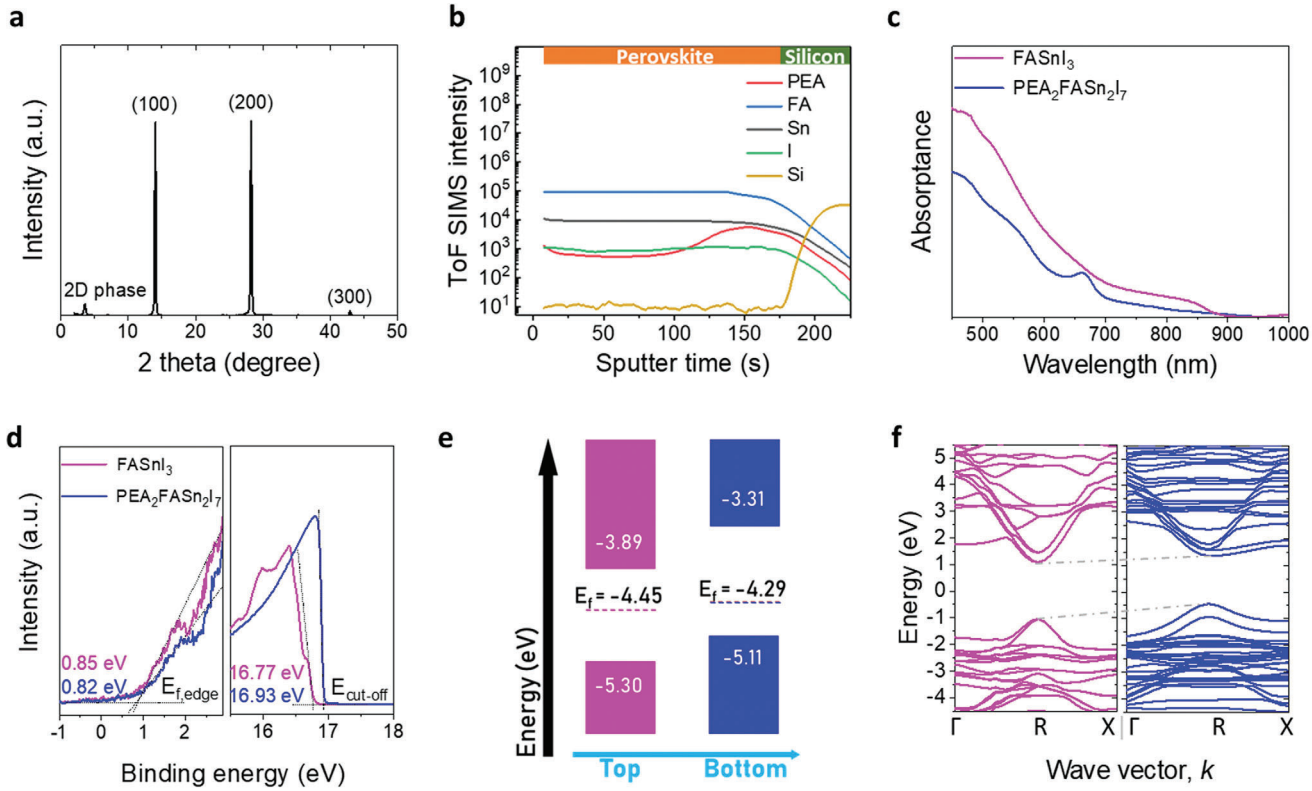

Figure 2. Properties of lead-free low-dimensional perovskite films. a) XRD patterns of the perovskite thin film prepared by $PEA_2FA_9Sn_{10}I_{31}$ precursor. b) ToF SIMS for passivate $PEA_2FA_9Sn_{10}I_{31}$ perovskite thin film. c) Absorption spectra of the $n = 2$ (2D) and $n =$ infinity (3D) perovskites. d) UPS measurements and e) the relative energy level diagram comparison of the 3D (purple) and 2D (blue) perovskites. f) The calculated band energy structures of the 3D (purple) and 2D (blue) perovskites, where the Fermi level is set as 0 eV.

As illustrated in Figure 2b, signals of Sn^{2+} and I^- in the sample are observed to be relatively constant throughout the entire perovskite film, indicating a uniform vertical distribution. Notably, the distribution of PEA^+ is predominantly concentrated at the bottom of the perovskite thin film, which confirms a vertical stratification between the bottom 2D and top 3D phases. This vertical compositional gradient with changes of PEA/FA ratios can be attributed to the smaller solubility of 3D $FASnI_3$ compared to that of 2D $PEA_2FASn_2I_7$ in the corresponding DMSO/DMF cosolvent.[52,71,72] Therefore, it is assumed that the 3D phase reaches supersaturation and precipitates out earlier than the 2D perovskite during downward grain growth, leading to the enrichment of 2D perovskite at the bottom. Furthermore, the crystallization kinetics are highly dependent on process conditions such as solvent drying speed. Thus, assisted by 8-min vacuum drying process for the wet perovskite film at a pressure of $\approx 10^{-2}$ bar, ultrafast evaporation of the DMSO/DMF cosolvent can lead to a more distinct separation of the 3D/2D phases and a different morphology than the previously reported intercalated 3D and 2D phases in the entire perovskite film.[73]

The pure 2D and 3D perovskite thin films were then characterized under the UV–vis–NIR absorption spectra analysis, respectively, as illustrated in Figure 2c. It can be observed that the absorption edges for the 2D and 3D perovskites are ≈690 and 880 nm, respectively. The energy bandgaps for the 2D and 3D perovskites are accurately determined to be 1.80 eV and 1.41 eV from Tauc plots of the absorption spectra in Figure S3 (Supporting Information). To gain a deeper understanding of the energy band alignment of the stacked 2D/3D heterojunction, ultraviolet photoelectron spectroscopy (UPS) measurements were performed on discrete 2D and 3D perovskites, respectively (Figure 2d). The Fermi edge ($E_{F,edge}$) and cut-off energy ($E_{cut\text{-}off}$) of the films were extracted, as shown in Figure 2e, revealing that the pure 2D perovskite film ($PEA_2FASn_2I_7$) has a higher VBM (-5.11 eV) than the 3D $FASnI_3$ film (-5.30 eV). Additionally, its CBM (-3.31 eV) is much higher than that of $FASnI_3$ (-3.89 eV). The 2D side of the 2D/3D heterojunction is closer to dielectric layer. Consequently, the cascaded band structure of the heterojunction is favorable for carrier separation under light illumination, leading to photo-generated holes accumulated in the bottom of the perovskite layer (2D phase) while electrons in the top surface (3D phase) as shown in Figure S4 (Supporting Information). Such a band structure effectively inhibits carrier recombination within the perovskite films. In conjunction with the inherent p-type channel of the 2D/3D perovskite heterojunction, the notably high relative dielectric constant (≈60) of the perovskite material, surpassing that of organic semiconductors (3) or silicon (11.9),[74–76] enhances the gating effect in the phototransistors.

2.2. Theoretical Calculations of Perovskites

As photoelectric conversion materials, the electronic structure of a perovskite plays a significant role in determining its spectral absorption property. To gain insight into the unique nature of the perovskite thin films, computational methods were carried out using the Vienna Ab initio Simulation Package (VASP) to investigate their energy band levels. The energy bandgap between the valence band maxima (VBM) and conduction band minima (CBM) of 3D $FASnI_3$ and 2D $PEA_2FASn_2I_7$ was determined using first-principles density-functional theory (DFT) calculation. The HSE hybrid function, which merges the exchange-correlation energy functional in DFT with Hartree-Fock (HF) theory, was then employed to calculate the values, and they were found to closely match experimental measurements (Figure S5, Supporting Information).[52] As shown in Figure 2f, the 2D and 3D perovskites show different bandgap energies, which is consistent with the UPS measurements.

The dielectric function $\varepsilon(\omega)$ is a useful tool for describing the spectral response of photoelectric materials, which can be described by the complex dielectric function:[77]

$$\varepsilon(\omega) = \varepsilon_r(\omega) + i\varepsilon_l(\omega) \quad (1)$$

where $\varepsilon_r(\omega)$ and $\varepsilon_l(\omega)$ are the real and imaginary parts of the dielectric function, respectively, which depend on the wavelength as shown in Figure S6 (Supporting Information). Using VASPKIT, the optical absorption coefficients (Figure S7, Supporting Information) of these compounds were calculated and found to be consistent with their experimental absorption spectra (Figure 2c) and previously calculated energy bandgaps (Figure 2f). Notably, the absorption coefficient was found to be as high as 10^5 cm^{-1}, mainly due to the absorption between the p orbitals of halide ions I in the valence band and the s-orbital of Sn in the conduction band.[78] The density of states (DOS) of these perovskite materials was also simulated (Figure S8, Supporting Information), providing an intuitive picture of bandgap engineering in perovskites, where the VBM and CBM are dominated by $[SnI_6]^{4-}$ layers in both 2D and 3D phases.

2.3. Perovskite Phototransistors

Perovskite phototransistors were fabricated with a device structure depicted in **Figure 3a**. The preparation processes began with the deposition of Cr (10 nm)/Au (80 nm) electrodes on SiO_2/n^+-Si substrates via photolithography and magnetron sputtering, along with the channel width/length of 800/4 µm. Afterward, perovskite films were deposited by spin-coating perovskite precursor solutions onto the substrates, followed by anti-solvent treatment and vacuum drying.

To evaluate the thickness effect of the perovskite layers of transistors for defect passivation, transfer and output curves of the devices fabricated with 0.6, and 0.9 $_M$ $PEA_2FA_9Sn_{10}I_{31}$ precursors were characterized at a drain voltage (V_{DS}) of 0.5 V in the dark, as displayed in Figures S9 and S10 (Supporting Information). Film thicknesses of ≈125 and 210 nm for 0.6 and 0.9 $_M$ precursors, respectively, were revealed by scanning electron microscope (SEM) cross-sectional images, as depicted in Figure S11 (Supporting Information). The channel currents (I_{DS}) of the devices increase with the decrease of gate voltage (V_g), indicating that the devices are p-channel transistors. It aligns well with the energy band diagram of the vertical 2D/3D heterostructure and the charge transfer behavior across the 2D phase during the photogating process (Figure S12, Supporting Information). Notably, the linear output curves of the devices under low V_{DS} indicate a good Ohmic contact at the perovskite/electrode interface, which is favorable for carrier transfer in the devices.

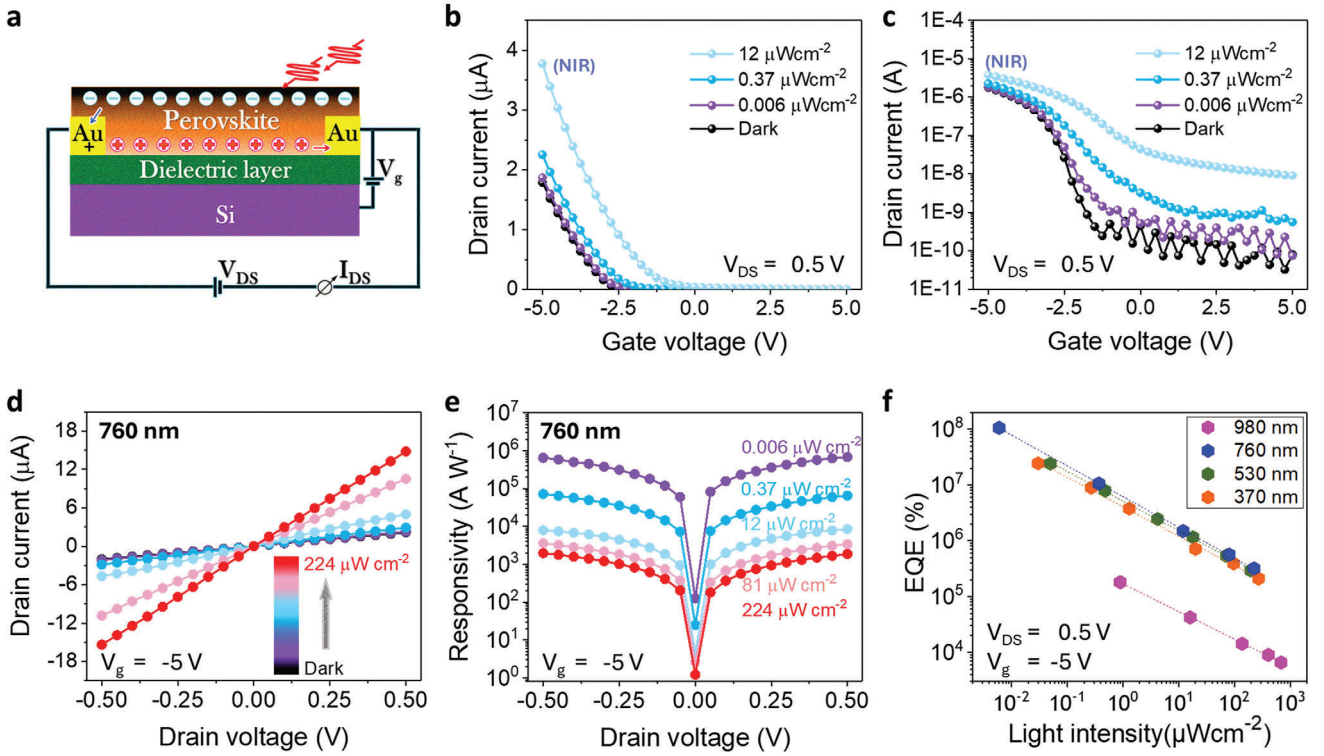

Figure 3. a) Schematic illustration of the perovskite phototransistor. b) Linear and c) semilog plots of I_{DS} of the optimized perovskite transistor (n = 10) with a Si_3N_4 dielectric layer against V_g under dark and various illumination power at 760 nm. Plots of d) I_{DS} and e) responsivity of the device as functions of V_{DS} under various NIR illumination power at V_g of -5 V. f) Plots of *EQE* as a function of light intensity at V_{DS} of 0.5 V and V_g of -5 V.

Then the effect of C—H—C treatment on perovskite films was characterized. The device based on a thicker perovskite film prepared from the 0.9 $_M$ precursor demonstrates negligible improvement of the on current after the cleaning treatment while the device with a thinner perovskite channel prepared from the 0.6 $_M$ precursor shows obvious improvement in the hole mobility, which can be attributed to the factor that the solvents may not be able to penetrate a thick film over ~200 nm. Hence, the devices studied in the following experiments were prepared with 0.6 $_M$ precursor unless otherwise specified. Linear scale plots of the transfer characteristics (I_{DS} vs V_g) for the devices can be used to extract the threshold voltage, as shown in Figure S13 (Supporting Information). The field-effect mobility (μ_{FE}) is a crucial parameter for estimating the performance of perovskite transistors, which can be calculated using the following Equation (2):[79]

$$I_{DS} = -\frac{W}{L} C_i \mu_{FE}(V_g - V_{th}) V_{DS} \text{ for } |V_g - V_{th}| >> V_{DS} \quad (2)$$

where W and L represent the channel width and length of the device, respectively, and C_i is the gate insulator capacitance per unit area. V_{th} is the threshold voltage of the transistor. The estimated μ_{FE} values for n = 10 device treated with cleaning processes of 0, 10, 20, and 30 min (0.044, 0.079, 0.164, and 0.156 cm^2 V^{-1}s^{-1}) were higher than those for n = 2 device (0.001, 0.003, 0.042, and 0.098 cm^2 V^{-1}s^{-1}). Despite the substantial improvement in the on current exhibited by the treated n = 2 devices, their off current was considerably higher than that of n = 10 devices, exhibiting a lower on/off ratio than the latter. Notably, the off current of a device with pure 3D $FASnI_3$ perovskite was very high even under a positive gate voltage of 100 V (Figure S14, Supporting Information) due to the oxidation of the pure 3D $FASnI_3$ perovskite. In general, pure 3D $FASnI_3$ perovskite can be oxidized more easily in comparison with 2D/3D mixed perovskites.

The application of an additional 10-min healing treatment resulted in a further optimization of V_{th} of the perovskite transistor, as evidenced by the shift to a more negative value from ≈70 to -10 V (Figure S15a, Supporting Information). The removal of traps of n = 10 devices after a proper C—H—C-treatment enhanced the μ_{FE} value to 0.287 cm^2 V^{-1}s^{-1},[56,80,81] while the μ_{FE} value of C—H—C-treated 2D $PEA_2FASn_2I_7$ perovskite transistors is only 0.162 cm^2 V^{-1}s^{-1} (Figure S15b, Supporting Information). Moreover, the device stability is significantly improved by the surface treatment. We noticed that the non-treated transistor exhibited degraded performance when a high gate voltage was continuously applied for 3 h, as depicted in Figure S16 (Supporting Information). Conversely, the C—H—C-treated device shows stable performance under the same conditions presumably due to the enhanced quality of the thin film.

To enhance the performance of phototransistors, we have introduced a high-κ Si_3N_4 dielectric layer (thickness: 100 nm, κ = 7.5) in lieu of the conventional SiO_2 layer (thickness: 300 nm). This modification in structure led to a significant decrease in energy consumption, achieved by reducing the operational gate voltage from -100 to -5 V (Figure 3b), a level notably lower than

that of other Pb-based[22,24,82] and Sn-based[83–85] phototransistors. The semilog representation of the transfer characteristic in a dark environment reveals a remarkable on/off ratio approaching 10^5 within a gate voltage span of -5 to 5 V (Figure 3c). The field-effect mobility of the phototransistor featuring the perovskite/Si_3N_4/n^+-Si configuration was estimated to be 0.647 $cm^2 V^{-1}s^{-1}$, representing a notable increase compared to the original perovskite/SiO_2/ n^+-Si setup at 0.287 $cm^2 V^{-1}s^{-1}$, which can be attributed to the improved film quality of the perovskite layer on the Si_3N_4 surface.

The output characteristics of the perovskite phototransistor with Si_3N_4 dielectric layer under NIR light illumination at gate voltage of -5 V are further displayed in Figure 3d, suggesting that I_{DS} of the device increases with increasing light intensity as well as V_{DS}. The photocurrents ($I_{Ph} = I_{Light} - I_{Dark}$) of the device under varying light illumination at gate voltage of -5 V were calculated and presented in Figure S17 (Supporting Information). The data has been further plotted through $\log_{10}$ scale for photocurrent versus voltage and power intensity (Figure S18, Supporting Information) to clearly present the experimental results, especially focusing on the data with low light intensity. Then the key parameters of photodetectors, including responsivity, gain, specific detectivity, linear dynamic range, and external quantum efficiency, are extracted.

The responsivity (R) is a key parameter for a photodetector, and it is defined by the following Equation (3):[75]

$$R\ (A\ W^{-1}) = \frac{I_{Ph}}{E_e WL} \tag{3}$$

where E_e represents the light intensity. The perovskite phototransistor with Si_3N_4 dielectric layer show a high responsivity of 6.8 × 10^5 A W^{-1} (V_{DS} = 0.5 V, E_e = 0.006 μW cm^{-2}) (Figure 3e), which is several orders of magnitude higher than the majority reported for pure perovskite photodetectors (Table S1, Supporting Information).[17,58,84,86–93] With the increase of light intensity, the device responsivity slowly decreases to ≈10^3 A W^{-1}, which is a common phenomenon for a phototransistor.

The gain (G) of the phototransistor is calculated using Equation (4):[94]

$$G = \frac{Rhc}{e\lambda} \tag{4}$$

where h is the Planck's constant, c is the speed of light, e is the elementary charge, and λ is the wavelength of the incident light. The device's maximum G at NIR wavelengths is estimated to be 1.1 × 10^6, which can be attributed to the efficient separation of photogenerated electron-hole pairs in the gradient perovskite heterojunction. Here, photocarriers circulate multiple times in the channel before eventually recombining with opposite charges, resulting in a high gain.

Another crucial parameter for phototransistors is the specific detectivity (D^*), which is defined by[75,94–96]

$$D^* = \frac{(AB)^{1/2}}{NEP} \tag{5}$$

$$NEP = \frac{\bar{i_n^2}^{1/2}}{R} \tag{6}$$

where A is the effective area of the device channel, B is the bandwidth, NEP is the noise equivalent power, and $\bar{i_n^2}^{1/2}$ is the root mean square value of the noise current. As demonstrated in Figure S19 (Supporting Information), the noise level per unit bandwidth (1 Hz) of the perovskite transistor is measured to be ≈ 1.1 × 10^{-11} A $Hz^{-1/2}$. Consequently, the device's maximum specific detectivities (V_{DS} = 0.5 V, V_g = -5 V, E_e = 0.006 μW cm^{-2}) is 4.0 × 10^{14} Jones (cm $Hz^{1/2}$ W^{-1}) at 760 nm wavelength, which is also superior to most perovskite photodetectors previously reported (Table S1, Supporting Information).

To better characterize the linear weak-light response range, linear dynamic range (LDR) can be calculated as[97–100]

$$LDR\ \ (dB) = 20 \times \log \frac{P_{\max}}{P_{\min}} \tag{7}$$

where P_{max} and P_{min} is the highest and lowest light power respectively, at which the response of the device deviates from the linear response. Notably, device responsivity further exhibits a good linear relationship versus light intensity at 0.5 V operating bias as shown in Figure S20 (Supporting Information), presenting LDR larger than 91 dB.

External quantum efficiency (EQE) is another key criterion that can be expressed as[101,102]

$$EQE = R\frac{hc}{\lambda} \tag{8}$$

We have plotted EQE versus light intensity curves of the phototransistor under a low drain voltage of 0.5 V and a gate voltage of -5 V across a broad range of wavelengths including UV (370 nm), visible (530 nm) and NIR (760 and 980 nm) light (Figure 3f). EQE spectra as functions of drain voltage, characterized under a light intensity of ≈1 μW cm^{-2}, were plotted in Figure S21 (Supporting Information).[103] The perovskite phototransistor exhibits a broad spectral photoresponse range from the UV to NIR regions, including a response to NIR light beyond 1050 nm. The photodetector with a broad and sensitive photo response range is highly desirable for many practical applications.

2.4. Synaptic Perovskite Phototransistors

Information transfer between neurons in the brain is typically facilitated through the delivery of neurotransmitter across the pre- and post-synaptic cleft. To mimic this process in an artificial synapse, a light pulse can be applied as the input spike, and the resulting post-synaptic current (PSC) can be measured as shown in **Figure 4a**. Device structures can be classified into two categories: two-terminal memristors and three-terminal transistor memristors. Two-terminal devices that adjust conductance through electrical spikes offer a simple structure, ease of operation, and high integration density; however, they may lack the ability to perform simultaneous signal transmission and programming functions in artificial synapses.[104–106] In contrast, three-terminal transistors utilize a gate voltage for electrical modulation, enabling synaptic functionalities by adjusting the conduction pathway between the source and drain electrodes.[107,108] Furthermore, transistor-type devices can concentrate carriers in the channel to enhance synaptic performance, promising advancements in

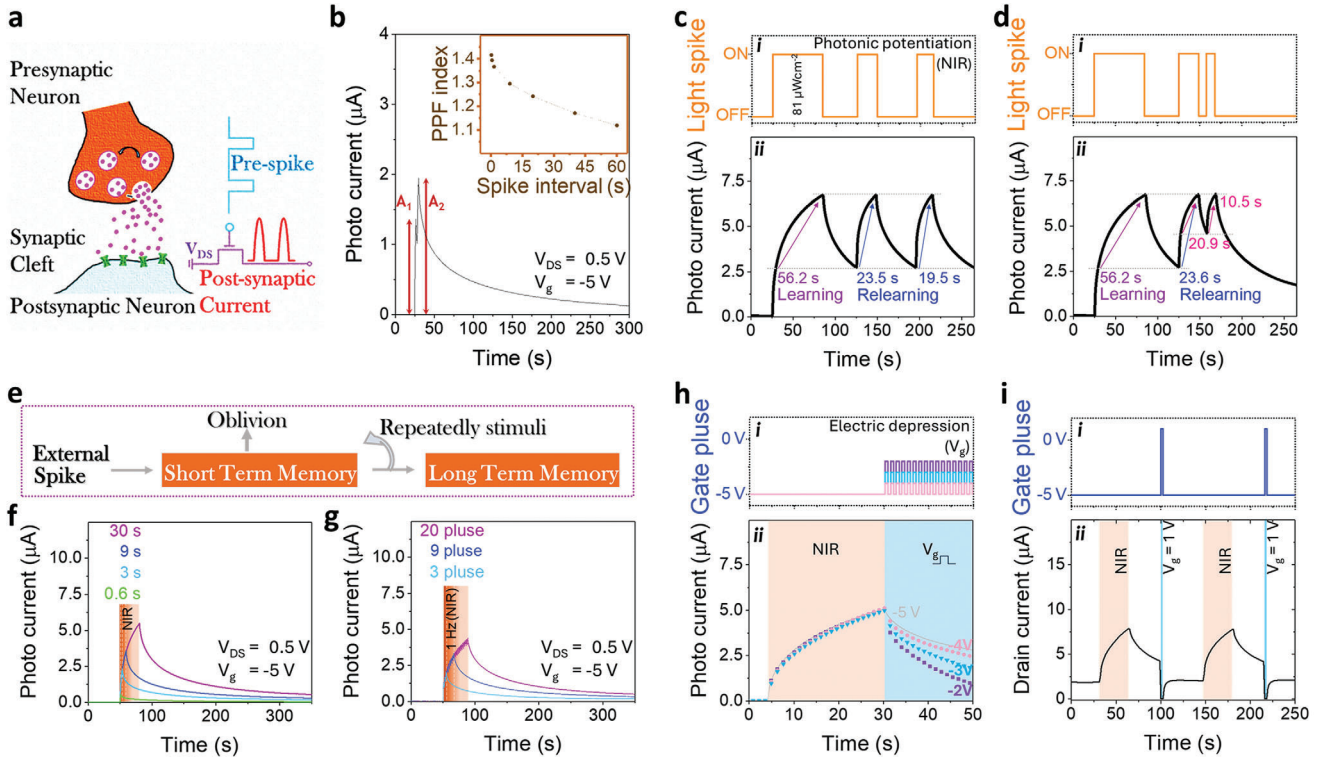

Figure 4. a) Schematic of biological synapse structure and artificial synapse device. b) Post-synaptic current (A_1 and A_2) with paired NIR light spikes (760 nm, 81 μW cm^{-2}) at V_{DS} of 0.5 V and V_g of -5 V. Inset: Paired pulse facilitation (PPF) behavior. c-d) Learning, forgetting and relearning behaviors emulated by the synaptic device. e) Memory consolidation schematic in human brain. F,g) Transition from STM to LTM through extended pulse duration and increased number of light pulses. h) Photonic potentiation with NIR illimitation and electric depression with negative gate pulses alternating between -5 V and -4/-3/-2 V. i) Memory erasure with positive gate pulse of 1 V.

next-generation brain-inspired neuromorphic computers characterized by large bandwidth, low energy consumption, and wireless communication capabilities.[39,40]

In our three-terminal light-stimulated synaptic transistor (LSST), the characteristic excitatory post-synaptic current (EPSC) was triggered by a presynaptic NIR light (760 nm; 81 μW cm^{-2}) and measured at a drain voltage of 0.5 V and gate voltage of -5 V. Given that perovskite material acts as both an efficient light-absorbing layer and carrier transport layer,[109–114] the photocurrent of our pure perovskite phototransistor can be weighted in proportion to the amount of light irradiation spike. By varying the interval, duration, and number of light pulses through photonic potentiation, it is feasible to precisely modulate the behavior of carriers within the perovskite channel. Figure 4b demonstrates the paired pulse facilitation (PPF) behavior induced by a pair of relatively pre-spikes, which depends on the extracted PPF index (A_2/A_1) on the interval time between two pulses (Δt).[115,116] Three sequences of light spikes were used to emulate learning-experience behavior, as shown in Figure 4c,d. The time interval required to reach the peak maximum value has been shortened with an increase in the number of light spikes. It is primarily a result of the decreasing trap density continuously filled by the photo-generated hole-electron pairs. After the first learning stage (56.2 s) and the subsequent spontaneous decay, the second learning stage required around one-third of the learning time (23.5 s) to achieve the same current level as under the first light stimuli, indicating a faster learning process due to prior exposure. Remarkably, the third learning stage could decrease the learning time even further (19.5 to 10.5 s), reflecting a form of information recollection process in a human brain.

In neuroscience, learning and memory consolidation in the human brain depend on both the intensity and frequency of learning. According to the reference literature,[117] Short-term memory (STM) is identified to last from milliseconds to minutes before reverting to its original state, while longer timescales are designated as long-term memory (LTM). Notably, LTM can be converted by STM through rehearsal learning processes (Figure 4e).[118–120] Similarly, our synaptic phototransistor exhibits both STM and LTM, as well as the transition from STM-to-LTM, by utilizing varying light pulse widths and numbers to emulate the learning duration and frequency. The change in channel conductance can be regarded as the memory level. Lengthening the duration of the light pulse from 0.6 to 30 s resulted in a higher photocurrent, indicating a stronger memory level, as illustrated in Figure 4f. Repetitive light spike stimuli can strengthen the memory level in this artificial synapse, facilitating the conversion from STM to LTM (Figure 4g). It is noted that their decay of the memory level following the stimuli initially decreased rapidly, followed by a slowdown, resembling the forgetting behaviors observed in a human brain.

Photo-generated holes tend to diffuse into the 2D perovskite layer of the heterojunction due to its energetic favorability, where

they transfer and recirculate numerous times within the bottom channel before recombining with opposite charges, as previously outlined (refer to Figure 2e,f; Figure S4, Supporting Information). Contrary to the previous approach, where a constant negative gate voltage of -5 V was employed to retain holes within the 2D perovskite layer to extend their recombination time, we have integrated negative gate pulses alternating between the initial -5 V and reduced levels of -4/-3/-2 V for specific electrical depression in the opto-synaptic device (Figure 4h). This integration has enriched the functionality of the device with controllable input stimuli that manage both light potentiation and gate depression. In addition, by utilizing a positive gate voltage to attract electrons into the p-type 2D perovskite layer of the heterojunction, recombination process could be prompted. Consequently, we have accomplished memory erasure by applying a low positive gate pulse of 1 V (Figure 4i), further enhancing the innovative potential of this synaptic device by significantly reducing the reset time for light stimuli.

3. Conclusion

In summary, we have successfully fabricated highly sensitive broadband phototransistors based on single layer 2D lead-free perovskites. The optimized device exhibited a high responsivity of up to 6.8×10^5 A W^{-1} under NIR light illumination, owing to the favorable compositional gradient that promotes efficient charge separation in the passivated perovskite layer. This value represents a substantial improvement over those reported for other perovskite photodetectors. Additionally, the device exhibits photo responses across a broad range of wavelengths, from UV to NIR, indicating its potential for a wide range of applications. The device capacity to achieve both short-term and long-term memory through the manipulation of light stimuli, in addition to electric depression and memory erasure, is a remarkable feature that has significant implications for the development of next-generation brain-inspired neuromorphic computers. These findings could pave the way for the creation of novel and efficient perovskite devices that have the potential to revolutionize a range of applications in the fields of optoelectronics and artificial intelligence.

4. Experimental Section

Perovskite Precursor Synthesis: $FASnI_3$, $PEA_2FASn_2I_7$, and $PEA_2FA_9Sn_{10}I_{31}$ precursor solutions were synthesized by mixing formamidinium iodide (FAI, Great cell Solar Ltd), tin iodide (SnI_2, Alfa Aesar), and phenethylammonium iodide (PEAI, Greatcell Solar Materials Ltd) in a dimethyl sulfoxide (DMSO, Sigma-Aldrich)/N,N-dimethylformamide (DMF, Alfa Aesar) (1:4, volume ratio) mixture at a concentration of 0.6 and 0.9 $_M$. To enhance the crystallinity and stability of the perovskite films, tin fluoride (SnF_2, Sigma Aldrich) and guanidinium thiocyanate (GuaSCN, Sigma Aldrich) were added to the precursor solutions at a molar ratio of 10% and 5%, respectively, to SnI_2. After preparation, the precursor solutions with additional Sn powder were stirred in a nitrogen-filled glovebox overnight and filtered with 0.45 µm polytetrafluoroethylene (PTFE) filters before use.

Pristine Perovskite Deposition for Photodetectors: The Si/SiO_2 (300 nm) and Si/Si_3N_4 (100 nm) substrates were subjected to ultrasonic cleaning in deionized water, acetone, and isopropyl alcohol (IPA) and dried with nitrogen gas. Photolithography and magnetron sputtering were used to pattern Cr (10 nm)/Au (80 nm) electrodes with a channel width (W) of 800 µm and a length (L) of 4 µm on the clean substrates. In cases where the anti-solvent method was employed during the perovskite thin film fabrication, the substrates were exposed to O_2 plasma for 5 min before spin-coating in a nitrogen-filled glovebox. The precursor solutions were then dropped onto the substrates, followed by a one-step spin-coating process at 2000 rpm for 3 s and 5000 rpm for 40 s. At the 30th second during the second spinning process, chlorobenzene (CB) was dripped as the anti-solvent. The wet perovskite films were immediately placed in an antechamber and pumped for 8 min at a pressure of $\approx 10^{-2}$ bar. After that, the samples were annealed at 70 °C for 10 min in a glovebox to induce better crystallization.

Solution-Processed Surface Treatment: To prepare the cleaning solvent, a mixture of polar tert-amyl alcohol (Sigma-Aldrich) and nonpolar cyclohexane (Sigma-Aldrich) was used in a volume ratio of 1:4. The healing solution was then prepared by dissolving 0.2 mg mL^{-1} FAI in the cleaning solvent. The cleaning process involved immersing the pristine perovskite substrates in 5 mL of the cleaning solvent in a glovebox for 10 min. The subsequent healing step was applied by immersing the cleaned samples in 5 mL of the healing solution for 10 min. Finally, the samples were immersed in 5 mL of the cleaning solvent for 10 min as a final cleaning step. Afterward, the healed perovskite substrates were dried under vacuum for 10 min. The C-treated samples were applied by immersing in the cleaning solvent for 10, 20, and 30 min, followed by vacuum drying.

Materials Characterization: The X-ray diffractometer (XRD, Rigaku SmartLab) was utilized to confirm the composition and orientation of the perovskites. The cross-sectional SEM images were examined using a field emission scanning electron microscope (Tescan MAIA3). The absorption spectra were recorded using a UV-VIS-NIR spectrometer (Perkin Elmer). Ultraviolet photoelectron spectroscopy (UPS, Thermo Fisher) was characterized using a Nexsa surface analysis system that was equipped with a He-discharge lamp that provided He-I photons at 21.22 eV. To determine the depth profile analysis of the perovskite films, a time-of-flight secondary ion mass spectrometry spectrometer (ToF-SIMS, GmbH) was used.

DFT Calculation: First-principles calculations utilizing Density Functional Theory (DFT) were performed using the Vienna Ab initio Simulation Package (VASP) version 5.4.4. To accurately model the electron-ion interactions, projector augmented-wave (PAW) pseudopotentials were employed. The Perdew, Burke, and Ernzerhof (PBE) functional, along with the hybrid functional Heyd-Scuseria-Ernzerhof (HSE), which combines PBE with the Hartree-Fock (HF) method, were utilized to account for the exchange-correlation interaction between electrons during the calculations.

Electrical, Optoelectronic Measurements for the Devices: The photoresponse measurements were carried out with a semiconductor parameter analyzer (Keithley 4200-SCS, Solon, Ohio, USA) under light illumination at various intensities in a glovebox. LEDs at specific wavelengths were utilized as the light sources for the measurements.

Supporting Information

Supporting Information is available from the Wiley Online Library or from the author.

Acknowledgements

H.-L. L. and T. W. contributed equally to this work. This work was supported by the Research Grants Council of Hong Kong, China (Project No. 15306822) and the Hong Kong Polytechnic University, Hong Kong, China (ZE2X). This work was also supported by the National Key R&D Program of China (Project No. 2023YFE0210800) and the Innovation and Technology Fund – Mainland-Hong Kong Joint Funding Scheme (Project No. MHP/004/23).

Conflict of Interest

The authors declare no conflict of interest.

Data Availability Statement

The data that support the findings of this study are available from the corresponding author upon reasonable request.

Keywords

broadband, perovskites, phototransistors, responsivity, synapses

Received: November 15, 2024
Revised: December 30, 2024
Published online: January 9, 2025

[1] J. B. Barton, R. F. Cannata, S. M. Petronio, *Proc. SPIE* **2002**, *4721*, 37.
[2] J. Kallhammer, *Nat. Photon.* **2006**, *5*, 12.
[3] J. Schmitt, S. Xiang, K. Yung, *JOSA A* **1998**, *15*, 2288.
[4] W.-F. Cheong, S. A. Prahl, A. J. Welch, *IEEE J. Quantum Electron.* **1990**, *26*, 2166.
[5] K. Welsher, S. P. Sherlock, H. Dai, *Proc. Natl. Acad. Sci. U.S.A.* **2011**, *108*, 8943.
[6] M. Garcia, C. Edmiston, T. York, R. Marinov, S. Mondal, N. Zhu, G. P. Sudlow, W. J. Akers, J. Margenthaler, S. Achilefu, *Optica* **2018**, *5*, 413.
[7] H.-W. Liu, X.-X. Hu, K. Li, Y. Liu, Q. Rong, L. Zhu, L. Yuan, F.-L. Qu, X.-B. Zhang, W. Tan, *Chem. Sci.* **2017**, *8*, 7689.
[8] R. Yousefi, M. Mahmoudian, A. Sa´aedic, M. Cheraghizaded, F. Jamali-Sheinie, M. Azarangf, *Ceram. Int.* **2016**, *42*, 15209.
[9] G. Wu, R. Fu, J. Chen, W. Yang, J. Ren, X. Guo, Z. Ni, X. Pi, C. Z. Li, H. Li, *Small* **2018**, *14*, 1802349.
[10] K. H. Hendriks, W. Li, M. M. Wienk, R. A. Janssen, *J. Am. Chem. Soc.* **2014**, *136*, 12130.
[11] Z. Zheng, L. Gan, J. Zhang, F. Zhuge, T. Zhai, *Adv. Sci.* **2017**, *4*, 1600316.
[12] C. Xie, C.-K. Liu, H.-L. Loi, F. Yan, *Adv. Funct. Mater.* **2019**, *30*, 1903907.
[13] C. R. Kagan, D. B. Mitzi, C. D. Dimitrakopoulos, *Science* **1999**, *286*, 945.
[14] S. Chen, G. Shi, *Adv. Mater.* **2017**, *29*, 1605448.
[15] X. Hong, T. Ishihara, A. V. Nurmikko, *Phys. Rev. B* **1992**, *45*, 6961.
[16] L. Qian, Y. Sun, M. Wu, C. Li, D. Xie, L. Ding, G. Shi, *Nanoscale* **2018**, *10*, 6837.
[17] Y. Liu, Y. Zhang, Z. Yang, H. Ye, J. Feng, Z. Xu, X. Zhang, R. Munir, J. Liu, P. Zuo, Q. Li, M. Hu, L. Meng, K. Wang, D. M. Smilgies, G. Zhao, H. Xu, Z. Yang, A. Amassian, J. Li, K. Zhao, S. F. Liu, *Nat. Commun.* **2018**, *9*, 5302.
[18] A. Thote, I. Jeon, J.-W. Lee, S. Seo, H.-S. Lin, Y. Yang, H. Daiguji, S. Maruyama, Y. Matsuo, *ACS. Appl. Energy Mater.* **2019**, *2*, 2486.
[19] H. Lin, C. Zhou, Y. Tian, T. Siegrist, B. Ma, *ACS Energy Lett.* **2018**, *3*, 54.
[20] X. Zhang, G. Wu, S. Yang, W. Fu, Z. Zhang, C. Chen, W. Liu, J. Yan, W. Yang, H. Chen, *Small* **2017**, *13*, 1700611.
[21] Z. Cheng, J. Lin, *CrystEngComm* **2010**, *12*, 2646.
[22] F. Li, C. Ma, H. Wang, W. Hu, W. Yu, A. D. Sheikh, T. Wu, *Nat. Commun.* **2015**, *6*, 8238.
[23] M. Cao, Y. Zhang, Y. Yu, L. Jin, Y. Li, Z. Chen, Y. Che, H. Dai, G. Zhang, J. Yao, *Opt. Mater.* **2018**, *84*, 498.
[24] N. Cho, F. Li, B. Turedi, L. Sinatra, S. P. Sarmah, M. R. Parida, M. I. Saidaminov, B. Murali, V. M. Burlakov, A. Goriely, O. F. Mohammed, T. Wu, O. M. Bakr, *Nat. Commun.* **2016**, *7*, 13407.
[25] Y. Sun, C. Teng, D. Xie, L. Qian, M. Sun, *J. Phys. Chem. C* **2017**, *121*, 11665.
[26] A. Krishna, S. Gottis, M. K. Nazeeruddin, F. Sauvage, *Adv. Funct. Mater.* **2019**, *29*, 1806482.
[27] L. Mao, C. C. Stoumpos, M. G. Kanatzidis, *J. Am. Chem. Soc.* **2019**, *141*, 1171.
[28] Y. Chen, Y. Sun, J. Peng, J. Tang, K. Zheng, Z. Liang, *Adv. Mater.* **2018**, *30*, 1703487.
[29] J. Zhou, Y. Chu, J. Huang, *ACS Appl. Mater. Interfaces* **2016**, *8*, 25660.
[30] R. T. Dong, C. Y. Lan, X. W. Xu, X. G. Liang, X. Y. Hu, D. P. Li, Z. Y. Zhou, L. Shu, S. Yip, C. Li, S. W. Tsang, J. C. Ho, *ACS Appl. Mater. Interfaces* **2018**, *10*, 19019.
[31] T. Ji, H. Zhang, N. Han, W. Wang, B. Wu, G. Li, M. Fan, Z. Li, Y. Hao, F. Zhu, Y. Wu, Y. Cui, *J. Mater. Chem. C* **2020**, *8*, 1110.
[32] H.-L. Loi, J. Cao, X. Guo, C. K. Liu, N. Wang, J. Song, G. Tang, Y. Zhu, F. Yan, *Adv. Sci.* **2020**, *7*, 2000776.
[33] G. Y. Kim, K. Kim, H. J. Kim, H. S. Jung, I. Jeon, J. W. Lee, *EcoMat* **2023**, *5*, e12319.
[34] E. Jokar, L. Cai, J. Han, E. J. C. Nacpil, I. Jeon, *Chem. Mater.* **2023**, *35*, 3404.
[35] T. H. Chowdhury, Y. Reo, A. Yusoff, Y. Y. Noh, *Adv. Sci.* **2022**, *9*, 2203749.
[36] C.-K. Liu, Q. Tai, N. Wang, G. Tang, H.-L. Loi, F. Yan, *Adv. Sci.* **2019**, *6*, 1900751.
[37] C. K. Liu, Q. Tai, N. Wang, G. Tang, Z. Hu, F. Yan, *ACS Appl. Mater. Interfaces* **2020**, *12*, 18769.
[38] A. Waleed, M. M. Tavakoli, L. Gu, Z. Wang, D. Zhang, A. Manikandan, Q. Zhang, R. Zhang, Y. L. Chueh, Z. Fan, *Nano Lett.* **2017**, *17*, 523.
[39] F. Zhang, C. Li, Z. Li, L. Dong, J. Zhao, *Microsyst. Nanoeng.* **2023**, *9*, 16.
[40] S. Liu, Z. Cheng, M.-Y. Li, S. Liu, H. Lu, X. Wen, C. Wang, X. Ding, L. Wang, *Matter* **2024**, *7*, 2810.
[41] Z. Xiao, J. Huang, *Adv. Electron. Mater.* **2016**, *2*, 1600100.
[42] D. B. Strukov, G. S. Snider, D. R. Stewart, R. S. Williams, *Nature* **2008**, *453*, 80.
[43] L. Q. Zhu, C. J. Wan, L. Q. Guo, Y. Shi, Q. Wan, *Nat. Commun.* **2014**, *5*, 3158.
[44] K. Kim, C.-L. Chen, Q. Truong, A. M. Shen, Y. Chen, *Adv. Mater.* **2013**, *25*, 1693.
[45] Y. H. Liu, L. Q. Zhu, P. Feng, Y. Shi, Q. Wan, *Adv. Mater.* **2015**, *27*, 5599.
[46] H.-T. Peng, M. A. Nahmias, T. F. De Lima, A. N. Tait, B. J. Shastri, *IEEE J. Sel. Top. Quantum Electron.* **2018**, *24*, 1.
[47] P. R. Prucnal, B. J. Shastri, T. F. de Lima, M. A. Nahmias, A. N. Tait, *Adv. Opt. Photon.* **2016**, *8*, 228.
[48] M. Lee, W. Lee, S. Choi, J. W. Jo, J. Kim, S. K. Park, Y. H. Kim, *Adv. Mater.* **2017**, *29*, 1700951.
[49] J. Gong, H. Wei, J. Liu, L. Sun, Z. Xu, H. Huang, W. Xu, *Matter* **2022**, *5*, 1578.
[50] H. Wei, G. Yao, Y. Ni, L. Yang, J. Liu, L. Sun, X. Zhang, J. Yang, Y. Xiao, F. Zheng, *Adv. Funct. Mater.* **2023**, *33*, 2304000.
[51] J. Gong, H. Yu, X. Zhou, H. Wei, M. Ma, H. Han, S. Zhang, Y. Ni, Y. Li, W. Xu, *Adv. Funct. Mater.* **2020**, *30*, 2005413.
[52] T. Wang, H.-L. Loi, J. Cao, Z. Qin, Z. Guan, Y. Xu, H. Cheng, M. G. Li, C.-S. Lee, X. Lu, *Adv. Sci.* **2022**, *9*, 2200242.
[53] X. Zhang, G. Wu, W. Fu, M. Qin, W. Yang, J. Yan, Z. Zhang, X. Lu, H. Chen, *Adv. Energy Mater.* **2018**, *8*, 1702498.
[54] J. Tong, Z. Song, D. H. Kim, X. Chen, C. Chen, A. F. Palmstrom, P. F. Ndione, M. O. Reese, S. P. Dunfield, O. G. Reid, *Science* **2019**, *364*, 475.
[55] D. Zhao, Y. Yu, C. Wang, W. Liao, N. Shrestha, C. R. Grice, A. J. Cimaroli, L. Guan, R. J. Ellingson, K. Zhu, *Nat. Energy* **2017**, *2*, 17018.
[56] X.-J. She, C. Chen, G. Divitini, B. Zhao, Y. Li, J. Wang, J. F. Orri, L. Cui, W. Xu, J. Peng, S. Wang, A. Sadhanala, H. Sirringhaus, *Nat. Electron.* **2020**, *3*, 694.

[57] J. M. Frost, A. Walsh, *Acc. Chem. Res.* **2016**, *49*, 528.
[58] H.-L. Loi, J. Cao, C.-K. Liu, Y. Xu, M. G. Li, F. Yan, *Small* **2023**, *19*, 2205976.
[59] M. Rahil, R. M. Ansari, C. Prakash, S. S. Islam, A. Dixit, S. Ahmad, *Sci. Rep.* **2022**, *12*, 2176.
[60] Y. J. Heo, H. J. Jang, J. H. Lee, S. B. Jo, S. Kim, D. H. Ho, S. J. Kwon, K. Kim, I. Jeon, J. M. Myoung, *Adv. Funct. Mater.* **2021**, *31*, 2106974.
[61] Y. Ju, X. g. Wu, S. Huang, G. Dai, T. Song, H. Zhong, *Adv. Funct. Mater.* **2022**, *32*, 2108296.
[62] Y. Liao, H. Liu, W. Zhou, D. Yang, Y. Shang, Z. Shi, B. Li, X. Jiang, L. Zhang, L. N. Quan, *J. Am. Chem. Soc.* **2017**, *139*, 6693.
[63] Y. Dang, Y. Zhou, X. Liu, D. Ju, S. Xia, H. Xia, X. Tao, *Angew. Chem. Int. Ed. Engl.* **2016**, *55*, 3447.
[64] D. Cui, X. Liu, T. Wu, X. Lin, X. Luo, Y. Wu, H. Segawa, X. Yang, Y. Zhang, Y. Wang, L. Han, *Adv. Funct. Mater.* **2021**, *31*, 2100931.
[65] J. Zhou, S. Fu, S. Zhou, L. Huang, C. Wang, H. Guan, D. Pu, H. Cui, C. Wang, T. Wang, *Nat. Commun.* **2024**, *15*, 2324.
[66] L. Dai, Z. Deng, F. Auras, H. Goodwin, Z. Zhang, J. C. Walmsley, P. D. Bristowe, F. Deschler, N. C. Greenham, *Nat. Photonics* **2021**, *15*, 696.
[67] C. Zhang, S. Wu, L. Tao, G. M. Arumugam, C. Liu, Z. Wang, S. Zhu, Y. Yang, J. Lin, X. Liu, R. E. I. Schropp, Y. Mai, *Adv. Energy Mater.* **2020**, *10*, 2002004.
[68] J. Wang, H. Li, S. Meng, X. Ye, X. Fu, S. Chen, *RSC. Adv.* **2017**, *7*, 27024.
[69] R. Bandara, K. Jayawardena, S. Adeyemo, S. Hinder, J. Smith, H. Thirimanne, N. Wong, F. Amin, B. Freestone, A. Parnell, *J. Mater. Chem. C* **2019**, *7*, 8389.
[70] S. Joy, H. R. Atapattu, S. Sorensen, H. Pruett, A. B. Olivelli, A. J. Huckaba, A.-F. Miller, K. R. Graham, *J. Mater. Chem. A.* **2022**, *10*, 13278.
[71] J. Cao, H.-L. Loi, Y. Xu, X. Guo, N. Wang, C.-K. Liu, T. Wang, H. Cheng, Y. Zhu, M. G. Li, W. Y. Wong, F. Yan, *Adv. Mater.* **2021**, *34*, 2107729.
[72] D. Li, Z. Xing, L. Huang, X. Meng, X. Hu, T. Hu, Y. Chen, *Adv. Mater.* **2021**, *33*, 2101823.
[73] Y. Lin, Y. Fang, J. Zhao, Y. Shao, S. J. Stuard, M. M. Nahid, H. Ade, Q. Wang, J. E. Shield, N. Zhou, A. M. Moran, J. Huang, *Nat. Commun.* **2019**, *10*, 1008.
[74] M. A. Green, A. Ho-Baillie, H. J. Snaith, *Nat. Photonics* **2014**, *8*, 506.
[75] S. M. Sze, K. K. Ng, *Physics of Semiconductor Devices*, John Wiley & Sons, Hoboken, New Jersey **2006**.
[76] L. Gu, Z. Fan, *Light Sci. Appl.* **2017**, *6*, e17090.
[77] X. Diao, Y. Diao, Y. Tang, G. Zhao, Q. Gu, Y. Xie, Y. Shi, P. Zhu, L. Zhang, *Sci. Rep.* **2022**, *12*, 12633.
[78] A. Varadwaj, P. R. Varadwaj, K. Yamashita, *ChemSusChem* **2018**, *11*, 449.
[79] P. B. Shea, J. Kanicki, N. Ono, *J. Appl. Phys.* **2005**, *98*, 014503.
[80] Y. Shao, Y. Fang, T. Li, Q. Wang, Q. Dong, Y. Deng, Y. Yuan, H. Wei, M. Wang, A. Gruverman, *Energy Environ. Sci.* **2016**, *9*, 1752.
[81] Y. Yuan, J. Huang, *Acc. Chem. Res.* **2016**, *49*, 286.
[82] G. Wang, D. Li, H.-C. Cheng, Y. Li, C.-Y. Chen, A. Yin, Z. Zhao, Z. Lin, H. Wu, Q. He, *Sci. Adv.* **2015**, *1*, 1500613.
[83] H. Wang, Y. Chen, E. Lim, X. Wang, S. Yuan, X. Zhang, H. Lu, J. Wang, G. Wu, T. Lin, S. Sun, J. Wang, Y. Zhan, H. Shen, X. Meng, J. Chu, *J. Mater. Chem. C* **2018**, *6*, 12714.
[84] F. Zhang, M. Shao, C. Wang, W. Wen, W. Shi, M. Qin, H. Huang, X. Wei, Y. Guo, Y. Liu, *Adv. Mater.* **2024**, *36*, 2307326.
[85] C. Chen, X. Zhang, G. Wu, H. Li, H. Chen, *Adv. Opt. Mater.* **2017**, *5*, 1600539.
[86] H. L. Zhu, H. Lin, Z. Song, Z. Wang, F. Ye, H. Zhang, W. J. Yin, Y. Yan, W. C. H. Choy, *ACS Nano* **2019**, *13*, 11800.
[87] H. L. Zhu, Z. Liang, Z. Huo, W. K. Ng, J. Mao, K. S. Wong, W. J. Yin, W. C. Choy, *Adv. Funct. Mater.* **2018**, *28*, 1706068.
[88] Z. Han, W. Fu, Y. Zou, Y. Gu, J. Liu, B. Huang, D. Yu, F. Cao, X. Li, X. Xu, *Adv. Mater.* **2021**, *33*, 2003852.
[89] H. Liu, H. L. Zhu, Z. Wang, X. Wu, Z. Huang, M. R. Huqe, J. A. Zapien, X. Lu, W. C. Choy, *Adv. Funct. Mater.* **2021**, *31*, 2010532.
[90] X. Tang, H. Zhou, X. Pan, R. Liu, D. Wu, H. Wang, *ACS Appl. Mater. Interfaces* **2020**, *12*, 4843.
[91] M. Krishnaiah, S. Kim, A. Kumar, D. Mishra, S. G. Seo, S. H. Jin, *Adv. Mater.* **2022**, *34*, 2109673.
[92] J. Shen, W. Zhu, Z. Lian, A. Lin, S.-F. Shi, K. Yang, M. Li, D. Zhao, Y.-Y. Sun, J. Lian, *ACS Appl. Electron. Mater.* **2023**, *5*, 5291.
[93] D. Liu, Q. Wei, L. Zhuang, M. Liu, L. Zeng, H. Ren, M. Li, S. P. Lau, *Adv. Opt. Mater.* **2024**, *12*, 2302411.
[94] D. Shao, J. Gao, P. Chow, H. Sun, G. Xin, P. Sharma, J. Lian, N. A. Koratkar, S. Sawyer, *Nano Lett.* **2015**, *15*, 3787.
[95] X. Liu, L. L. Gu, Q. P. Zhang, J. Y. Wu, Y. Z. Long, Z. Y. Fan, *Nat. Commun.* **2014**, *5*, 4007.
[96] C. O. Kim, S. Kim, D. H. Shin, S. S. Kang, J. M. Kim, C. W. Jang, S. S. Joo, J. S. Lee, J. H. Kim, S.-H. Choi, *Nat. Commun.* **2014**, *5*, 3249.
[97] C. Li, H. Wang, F. Wang, T. Li, M. Xu, H. Wang, Z. Wang, X. Zhan, W. Hu, L. Shen, *Light Sci. Appl.* **2020**, *9*, 31.
[98] M. Jeong, S. G. Han, W. Sung, S. Kim, J. Min, M. K. Kim, W. Choi, H. Lee, D. Lee, M. Kim, *Adv. Funct. Mater.* **2023**, *33*, 2300695.
[99] W. Jang, K. Kim, B. G. Kim, J. S. Nam, I. Jeon, D. H. Wang, *Adv. Funct. Mater.* **2022**, *32*, 2207713.
[100] J. S. Nam, W. Jang, J. Han, B. G. Kim, J. H. Lim, D. Kim, I. Chung, D. H. Wang, I. Jeon, *Adv. Funct. Mater.* **2024**, *34*, 2407299.
[101] L. Li, F. Zhang, J. Wang, Q. An, Q. Sun, W. Wang, J. Zhang, F. Teng, *Sci. Rep.* **2015**, *5*, 9181.
[102] X. Hu, X. Zhang, L. Liang, J. Bao, S. Li, W. Yang, Y. Xie, *Adv. Funct. Mater.* **2014**, *24*, 7373.
[103] T. Kada, S. Asahi, T. Kaizu, Y. Harada, R. Tamaki, Y. Okada, T. Kita, *Sci. Rep.* **2017**, *7*, 5865.
[104] F. Zhou, Z. Zhou, J. Chen, T. H. Choy, J. Wang, N. Zhang, Z. Lin, S. Yu, J. Kang, H.-S. P. Wong, *Nat. Nanotechnol.* **2019**, *14*, 776.
[105] L. Mennel, J. Symonowicz, S. Wachter, D. K. Polyushkin, A. J. Molina-Mendoza, T. Mueller, *Nature* **2020**, *579*, 62.
[106] M. D. Tran, H. Kim, J. S. Kim, M. H. Doan, T. K. Chau, Q. A. Vu, J. H. Kim, Y. H. Lee, *Adv. Mater.* **2019**, *31*, 1807075.
[107] Q. Xia, M. D. Pickett, J. J. Yang, X. Li, W. Wu, G. Medeiros-Ribeiro, R. S. Williams, *Adv. Funct. Mater.* **2011**, *21*, 2660.
[108] C. Robert, *Nat. Commun.* **2020**, *11*, 3801.
[109] Z.-K. Tang, Z.-F. Xu, D.-Y. Zhang, S.-X. Hu, W.-M. Lau, L.-M. Liu, *Sci. Rep.* **2017**, *7*, 7843.
[110] L. Shen, Y. J. Fang, D. Wang, Y. Bai, Y. H. Deng, M. M. Wang, Y. F. Lu, J. S. Huang, *Adv. Mater.* **2016**, *28*, 10794.
[111] Y. C. Kim, K. H. Kim, D. Y. Son, D. N. Jeong, J. Y. Seo, Y. S. Choi, I. T. Han, S. Y. Lee, N. G. Park, *Nature* **2017**, *550*, 87.
[112] V. Adinolfi, O. Ouellette, M. I. Saidaminov, G. Walters, A. L. Abdelhady, O. M. Bakr, E. H. Sargent, *Adv. Mater.* **2016**, *28*, 7264.
[113] S. Shrestha, R. Fischer, G. J. Matt, P. Feldner, T. Michel, A. Osvet, I. Levchuk, B. Merle, S. Golkar, H. W. Chen, S. F. Tedde, O. Schmidt, R. Hock, M. Ruhrig, M. Goken, W. Heiss, G. Anton, C. J. Brabec, *Nat. Photonics* **2017**, *11*, 436.
[114] S. D. Stranks, G. E. Eperon, G. Grancini, C. Menelaou, M. J. P. Alcocer, T. Leijtens, L. M. Herz, A. Petrozza, H. J. Snaith, *Science* **2013**, *342*, 341.
[115] B. Huang, N. Li, Q. Wang, C. Ouyang, C. He, L. Zhang, L. Du, W. Yang, R. Yang, D. Shi, G. Zhang, *Adv. Mater. Interfaces* **2022**, *9*, 2201558.
[116] Y. T. Yang, Y. S. Wu, W. He, H. C. Tien, W. C. Yang, T. Michinobu, W. C. Chen, W. Y. Lee, C. C. Chueh, *Adv. Sci.* **2022**, *9*, 2203025.

[117] L. Abbott, W. G. Regehr, *Nature* **2004**, *431*, 796.
[118] J. Liu, Z. Yang, Z. Gong, Z. Shen, Y. Ye, B. Yang, Y. Qiu, B. Ye, L. Xu, T. Guo, S. Xu, *ACS Appl. Mater. Interfaces* **2021**, *13*, 13362.
[119] J. H. Kim, M. Stolte, F. Wurthner, *ACS Nano* **2022**, *16*, 19523.
[120] S. Dai, X. Wu, D. Liu, Y. Chu, K. Wang, B. Yang, J. Huang, *ACS Appl. Mater. Interfaces* **2018**, *10*, 21472.

